Squirt-flow seismic dispersion models: A comparison

Yongyang Sun[1*], José M. Carcione[2,3], Boris Gurevich[1]

[1] *Centre for Explorations Geophysics, Curtin University, GPO Box U1987, Perth, WA 6845, Australia.*

Email: yongyang.sun@postgrad.curtin.edu.au

[2] *Istituto Nazionale di Oceanografia e di Geofisica Sperimentale (OGS),*

Borgo Grotta Gigante 42c, 34010 Sgonico, Trieste, Italy.

[3] *School of Earth Sciences and Engineering, Hohai University, Nanjing, 211100, China.*

SUMMARY

The anelastic properties of porous rocks depend on the pore characteristics, specifically, the pore aspect ratio and the pore fraction (related to the soft porosity). At high frequencies, there is no fluid pressure communication throughout the pore space and the rock becomes stiffer than at low frequencies, where the pore pressure is fully equilibrated. This causes a significant difference between the moduli at low and high frequencies, which is known as seismic dispersion and is commonly explained by the squirt-flow mechanism. In this paper, we consider and contrast three squirt-flow dispersion models: the modified Mavko-Jizba model, valid for a porous medium with arbitrary shapes of the pores and cracks, and two other models, based on idealized geometries of spheres and ellipsoids: the EIAS (equivalent inclusion-average stress) and CPEM (cracks and pores effective medium) models. We first perform analytical comparisons and then compute several numerical examples to demonstrate similarities and differences between the models. The analytical comparison shows that when the stiff pores are spherical and the crack density is small, the theoretical predictions of the three models are very close to each other. However, when the stiff pores are spheroids with an aspect ratio smaller than 1

(say, between 0.2 and 1), the predictions of inclusion based models are not valid at frequencies of ultrasonic measurements on rock samples. In contrast, the predictions of the modified Mavko-Jizba model are valid at ultrasonic frequencies of about 10^6 Hz, which is a typical frequency of laboratory measurements on core samples. We also introduce Zener-based bulk and shear dispersion indices, which are proportional to the difference between the high- and low-frequency stiffness moduli, and are a measure of the degree of anelasticity, closely related to the quality factors by view of the Kramers-Kronig relations. The results show that the three models yield similar moduli dispersion with very small differences when the crack density is relatively high. The indices versus crack density can be viewed as a template to obtain the crack properties from low- and high-frequency velocity measurements.

Key words: Acoustic properties; Seismic attenuation; Microstructure.

1 INTRODUCTION

Wave propagation in rocks shows anelastic properties, namely, velocity dispersion and dissipation of energy depending on frequency (Jones 1986; Müller et al. 2010; Carcione 2014, e.g.). In many rocks the dispersion is caused by squirt flow, that is by fluid pressure equilibration between stiff pores, which occupies almost all the pore space, and soft pores or cracks, whose overall volume is very small but which strongly affect the overall rock moduli and are themselves sensitive to effective pressure (Walsh 1965; Zimmerman 1991; Zhang et al. 2019a,b, e.g.). At low frequencies, the pore fluid has enough time to equilibrate throughout the pore space, and the wet-rock moduli are given by Gassmann (1951) equations. Conversely, at high frequencies, there is not enough time for fluid pressure to equilibrate between soft and stiff pores, and hence the overall moduli become higher. The difference between low and high frequency moduli quantifies seismic dispersion (Mavko & Nur 1975; O'Connell & Budiansky 1977; Palmer & Traviola 1980; Murphy III et al. 1986; Dvorkin et al. 1995; Chapman et al. 2002; Pride et al. 2004; Alkhimenkov et al. 2020).

Several theoretical models have been proposed to quantify this dispersion. Mavko & Jizba (1991) proposed a model for so-called unrelaxed frame, whose soft pores are liquid saturated while stiff pores are dry. The moduli of the fully liquid-saturated rock are then computed using Gassmann equation (in which the dry bulk modulus is replaced with the modulus of the

unrelaxed frame). In the Mavko & Jizba (1991) (MJ) model, the pore fluid must be liquid, but Gurevich et al. (2009) generalized the MJ model to fluids of arbitrary bulk modulus. Similarly to Gassmann equation, both the original MJ model and the generalized version of Gurevich et al. (2009) (MJG) do not depend on the parameters of the pore space, such as aspect ratios, explicitly.

In contrast, the Equivalent Inclusion-Average Stress (EIAS) model (Endres & Knight 1997) and the Crack-Pores Effective Medium(CPEM) model (Adelinet et al. 2011) use effective medium theory designed for elastic media with pores and cracks of oblate spheroidal shape, and their predictions explicitly depend on these aspect ratios and volume fractions of these pores and cracks. Thus, the question arises as to whether their predictions are the same or similar. Neither Endres & Knight (1997) not Adelinet et al. (2011) compare their results to the MJ model. Adelinet et al. (2011) numerically compared the CPEM results to the EIAS results and found a significant discrepancy, which they attribute to the use of Kuster & ToksÃűz (1974) model (KT) in the EIAS. This explanation is unconvincing as both Kachanov (1993) and KT models are based on the same Eshelby (1957) theory.

In general, it is extremely difficult to observe dispersion in seismic or acoustic field data due to limited frequency range of field data, which seldom cover more than one decade in frequency. However dispersion is directly related to attenuation, which is known to affect seismic and acoustic field data. Precise dependence of attenuation on frequency is controlled by details of the pore shape distribution. However, the Zener or standard-linear solid model(Carcione 2014, e.g.) provides a precise mathematical relation between the amount of dispersion and the minimum quality factor, Q_0, of the relaxation peak, or equivalently, the maximum dissipation factor, Q_0^{-1}. The model satisfies the Kramers-Kronig relations (Carcione et al. 2019). We introduce here the bulk and shear dispersion indices based on the Zener model, which are proportional to the difference between the high- and low-frequency stiffness moduli, and are a measure of the degree of anelasticity. The associated quality factor is that of the Zener model, which is a good representation of the relaxation peaks related to the squirt-flow attenuation mechanism, by which flow from fluid-filled microcracks (and grain contacts) to the stiff pore space and vice versa, induces energy dissipation (Carcione & Gurevich 2011). Biot (1962) was the first to discuss this mechanism and proposed a viscoelastic mechanical model to describe it.

In this paper, we perform a detailed analytical comparison of the dispersion predicted by the three models, CPEM, MJ with its generalization MJG and EIAS with its dilute approximation, and illustrate their similarities and differences by numerical examples. Plots of

the dispersion indices as a function of the crack fraction and aspect ratio can be viewed as templates to obtain these properties from low- and high-frequency velocity measurements.

2 THE DISPERSION MODELS

We study three models, namely, the generalized MJ model (Mavko & Jizba 1991; Gurevich et al. 2009), the EIAS model by Endres & Knight (1997) and CPEM model of Adelinet et al. (2011). In the EIAS and CPEM models, the medium under study consists on an isotropic distribution of pores or cracks, respectively spheres and spheroids, whereas the MJ model considers pores and cracks of of more general shapes (with aspect ratio on the order of 1 for pores and $\ll 1$ for cracks). Here, the crack fraction is denoted by c and the aspect ratio by a.

The EIAS and CPEM models yield the low-frequency bulk and shear moduli, K_0 and μ_0, and the high-frequency bulk and shear moduli, K_∞ and μ_∞, as functions of the aspect ratio and crack fraction. Both models have their root in the work of Eshelby (1957). The physics behind these inclusion-based models is as follows. A wave induces a higher fluid pressure in the cracks and the excess pressure is relieved to the spherical pores, so that $K_\infty > K_0$. This effect increases as the crack aspect ratio decreases.

2.1 The EIAS model

Endres & Knight (1997) assume that the stiff pores are spheres and the soft pores are spheroidal (penny-shaped) cracks of aspect ratio $a \ll 1$. At high frequencies they assume that cracks are hydraulically isolated from the pores. The corresponding moduli K_∞ and μ_∞ predicted by Endres & Knight (1997)(equations (32) and (33)), are

$$\begin{aligned} K_\infty &= K_s + \frac{\phi(K_f - K_s)\gamma}{1-\phi(1-\gamma)}, \\ \mu_\infty &= \frac{\mu_s(1-\phi)}{1-\phi(1-\chi)}, \end{aligned} \tag{1}$$

where K_f is the fluid bulk modulus, ϕ is the total porosity, and

$$\begin{aligned} \gamma &= (1-c)P_1 + cP_2, \\ \chi &= (1-c)Q_1 + cQ_2 \end{aligned} \tag{2}$$

(Endres & Knight 1997, equations (54) and (55)) with

$$
\begin{aligned}
P_1 &= \frac{K_s + 4\mu_s/3}{K_f + 4\mu_s/3}, \\
P_2 &= \frac{K_s}{K_f + \pi a \beta}, \quad \beta = \mu_s \cdot \frac{3K_s + \mu_s}{3K_s + 4\mu_s} \\
Q_1 &= 1 + \mu_s/\zeta, \quad \zeta = \frac{\mu_s}{6} \cdot \frac{9K_s + 8\mu_s}{K_s + 2\mu_s}, \\
Q_2 &= \frac{1}{5}\left[1 + \frac{8\mu_s}{\pi a(\mu_s + 2\beta)} + 2 \cdot \frac{K_f + 2\mu_s/3}{K_f + \pi a \beta}\right],
\end{aligned}
\tag{3}
$$

where P_1 and Q_1 correspond to spherical (stiff) pores and P_2 and Q_2 to penny-shaped (soft) cracks, with very low aspect ratios. Coefficients P_2 and Q_2 are approximations for $a \ll 1$. K_s and μ_s are the bulk and shear moduli of the grains.

At low frequencies, Endres & Knight (1997) assume complete fluid pressure communication between pores and cracks, the effective moduli are (Endres & Knight 1997, equations (34) and (35)),

$$
\begin{aligned}
K_0 &= K_s + \frac{\phi K_s (K_f - K_s)\gamma_0}{(1-\phi)(K_s - K_f) + [K_f + \phi(K_s - K_f)]\gamma_0}, \\
\mu_0 &= \frac{\mu_s(1-\phi)}{1 - \phi(1 - \chi_0)},
\end{aligned}
\tag{4}
$$

where γ_0 and χ_0 corresponds to the values of γ and χ when $K_f = 0$.

The EIAS model is consistent with the Hashin-Shtrikman bounds when applied to two-phase systems regardless of the pore shape spectrum. It has no restrictions on the crack density, since it includes interactions between cracks in some form. Endres & Knight (1997) also developed a dilute approximation given by their equations (48)-(51). We refer to this dilute EIAS model as EIASD. Since both MJ and CPEM models assume a dilute concentration of cracks, the EIASD model is more suitable for comparison with these other models. The high-frequency wet moduli predicted by the EIASD model are

$$
\begin{aligned}
K_\infty &= \frac{K_s^2}{K_s + \phi(K_s - K_f)\gamma} \\
\mu_\infty &= \frac{\mu_s}{1 + \phi\chi},
\end{aligned}
\tag{5}
$$

where γ and χ are given in equation (2). Taylor expansion of the r.h.s of equations (1) and (5) in powers of ϕ shows that they coincide for $\phi \ll 1$.

2.2 The CPEM model

An alternative dispersion model was porposed by Adelinet et al. (2011), who also describe the pore space by a combination of spherical pores and penny-shaped cracks. Their high-frequency wet-rock moduli are given by

$$\frac{K_s}{K_\infty} = 1 + \phi_p \frac{3(1-\nu_s)}{2(1-2\nu_s)} \left(\frac{\delta_p}{1+\delta_p} \right) + \frac{16(1-\nu_s^2)}{9(1-2\nu_s)} \left(\frac{\delta_c}{1+\delta_c} \right) \epsilon \tag{6}$$

and

$$\frac{\mu_s}{\mu_\infty} = 1 + \phi_p \frac{15(1-\nu_s)}{7-5\nu_s} + \left[\frac{16(1-\nu_s)}{15(1-0.5\nu_s)} + \frac{32(1-\nu_s)}{45} \left(\frac{\delta_c}{1+\delta_c} \right) \right] \epsilon, \tag{7}$$

where $\phi_p = \phi(1-c)$ is the stiff porosity,

$$\delta_p = \frac{2Y_s}{9(1-\nu_s)} \left(\frac{1}{K_f} - \frac{1}{K_s} \right), \quad \delta_c = \frac{\pi Y_s a}{4(1-\nu_s^2)} \left(\frac{1}{K_f} - \frac{1}{K_s} \right), \tag{8}$$

and

$$Y_s = \frac{9K_s\mu_s}{3K_s+\mu_s} \quad \text{and} \quad \nu_s = \frac{3K_s - 2\mu_s}{2(3K_s+\mu_s)} \tag{9}$$

are the mineral Young modulus and Poisson ratio, respectively. ϵ is the crack density defined by

$$\epsilon = \frac{3\phi_c}{4\pi a} = \frac{3\phi c}{4\pi a} \tag{10}$$

(Gurevich 2003, equation (36)), where $\phi_c = \phi c$ is the soft porosity.

The high-frequency dry-rock moduli, K_{m0} and μ_{m0}, can be obtained from equations (6) and (7) by taking $\delta_p \to \infty$ and $\delta_c \to \infty$, so that $\delta_p/(1+\delta_p) = 1$ and $\delta_c/(1+\delta_c) = 1$. The low-frequency wet-rock moduli K_0 and μ_0 are given by Gassmann equations

$$K_0 = \frac{K_s - K_{m0} + \phi K_{m0}\,(K_s/K_f - 1)}{1 - \phi - K_{m0}/K_s + \phi K_s/K_f} \quad \text{and} \quad \mu_0 = \mu_{m0}, \tag{11}$$

where K_{m0} and μ_{m0} are the high-frequency dry-rock moduli previously obtained. Actually, the low and high-frequency dry-rock moduli are identical (no dispersion in dry rock, Adelinet et al. (2011)).

2.3 Mavko-Jizba moduli

Mavko & Jizba (1991) proposed a model for squirt dispersion in cracked rocks, where the main results are the so-called unrelaxed frame bulk and shear moduli, $K_{m\infty}$ and $\mu_{m\infty}$, obtained under an assumption that the stiff pores are dry but the soft (compliant) pores are filled with a fluid.

The unrelaxed frame bulk and shear moduli $K_{m\infty}$ and $\mu_{m\infty}$ are given by

$$\frac{1}{K_{m\infty}} \approx \frac{1}{K_h} + \left(\frac{1}{K_f} - \frac{1}{K_s}\right)\phi_c \tag{12}$$

and

$$\frac{1}{\mu_{m\infty}} = \frac{1}{\mu_{m0}} - \frac{4}{15}\left(\frac{1}{K_{m0}} - \frac{1}{K_{m\infty}}\right), \tag{13}$$

where K_h is the dry bulk modulus of the rock without soft porosity (without cracks).

However, the MJ model is only valid for liquid-saturated rocks. For rocks with much softer fluids (e.g., gas), Gurevich et al. (2009) generalized equation (12) to

$$\frac{1}{K_{m\infty}} = \frac{1}{K_h} + \frac{1}{\dfrac{1}{\dfrac{1}{K_{m0}} - \dfrac{1}{K_h}} + \dfrac{1}{\left(\dfrac{1}{K_f} - \dfrac{1}{K_s}\right)\phi_c}}. \tag{14}$$

while shear modulus is given by the same equation (13).

Then, the high-frequency wet-rock bulk and shear moduli are given by Gassmann equations,

$$K_\infty = \frac{K_s - K_{m\infty} + \phi K_{m\infty}\left(K_s/K_f - 1\right)}{1 - \phi - K_{m\infty}/K_s + \phi K_s/K_f} \quad \text{and} \quad \mu_\infty = \mu_{m\infty}. \tag{15}$$

Effectively, the unrelaxed frame consists of two "minerals", the original mineral and the fluid in the cracks, but strictly speaking, this system is not actually Gassmann consistent and the full Brown-Korringa extension for mixed mineralogy should be used (Brown & Korringa 1975). Usually, this approach is impractical as there is no rigorous recipe to define the extra constant.

3 ANALYTICAL COMPARISON OF DISPERSION MODELS

In this section, we perform a detailed analytical comparison of the dispersion predicted by the three models and illustrate their similarities and differences. We first compare one of inclusion-based models, CPEM, against the MJG model, and then show that the moduli predicted by the two inclusion-based models are almost identical.

3.1 Comparison between the CPEM and MJG models

3.1.1 Bulk modulus

As discussed above, the MJG model relates the high-frequency modulus of the saturated rock to the dry-rock modulus of the same rock but without cracks. To obtain a similar relationship from the CPEM model, we note that the dry-rock bulk modulus K_{m0} can be obtained from equation (6) by taking $\delta_p \to \infty$ and $\delta_c \to \infty$,

$$\frac{K_s}{K_{m0}} = \frac{K_s}{K_h} + \frac{16(1-\nu_s^2)}{9(1-2\nu_s)}\epsilon, \tag{16}$$

where

$$\frac{K_s}{K_h} = 1 + \frac{3(1-\nu_s)}{2(1-2\nu_s)}\phi_p. \tag{17}$$

Here, we have used the identity

$$\frac{16(1-\nu_s^2)}{9(1-2\nu_s)}\epsilon\delta_c = \frac{\phi_c Y_s}{3(1-2\nu_s)}\left(\frac{1}{K_f}-\frac{1}{K_s}\right) = \phi_c K_s\left(\frac{1}{K_f}-\frac{1}{K_s}\right). \tag{18}$$

which follows from the second equation (8) and the definition of crack density (10).

The bulk modulus of the unrelaxed frame $K_{m\infty}$ can be obtained from equation (6) by assuming that the stiff pores are dry, and hence $\delta_p \to \infty$,

$$\frac{K_s}{K_{m\infty}} = \frac{K_s}{K_h} + \frac{16(1-\nu_s^2)}{9(1-2\nu_s)}\epsilon\left(\frac{\delta_c}{1+\delta_c}\right). \tag{19}$$

or

$$\frac{K_s}{K_{m\infty}} = \frac{K_s}{K_h} + \left[\frac{1}{\frac{16(1-\nu_s^2)}{9(1-2\nu_s)}\epsilon} + \frac{1}{\frac{16(1-\nu_s^2)}{9(1-2\nu_s)}\epsilon\delta_c}\right]^{-1}. \tag{20}$$

Using (16) and (18), equation (20) becomes

$$\frac{1}{K_{m\infty}} = \frac{1}{K_h} + \frac{1}{\frac{1}{\left(\frac{1}{K_{m0}}-\frac{1}{K_h}\right)} + \frac{1}{\phi_c\left(\frac{1}{K_f}-\frac{1}{K_s}\right)}}. \tag{21}$$

This equation is identical to the MJG equation (14) in form.

Rewriting (6) as

$$\frac{K_s}{K_\infty} = 1 + \phi_p\frac{3(1-\nu_s)}{2(1-2\nu_s)}\left(\frac{\delta_p}{1+\delta_p}\right) + \left[\frac{1}{\frac{16(1-\nu_s^2)}{9(1-2\nu_s)}\epsilon} + \frac{1}{\frac{16(1-\nu_s^2)}{9(1-2\nu_s)}\epsilon\delta_c}\right]^{-1}, \tag{22}$$

we obtain

$$\frac{1}{K_\infty} = \frac{1}{K_h^{sat}} + \frac{1}{\frac{1}{\left(\frac{1}{K_{m0}}-\frac{1}{K_h}\right)} + \frac{1}{\phi_c\left(\frac{1}{K_f}-\frac{1}{K_s}\right)}}, \tag{23}$$

where K_h^{sat} is the bulk modulus of the fluid-saturated rock without soft porosity (without cracks),

$$\frac{K_s}{K_h^{sat}} = 1 + \phi_p\frac{3(1-\nu_s)}{2(1-2\nu_s)}\left(\frac{\delta_p}{1+\delta_p}\right). \tag{24}$$

Equations (23) and (21) are similar. Indeed, the second terms in the right-hand sides of the

two equations are identical. The difference is that equation (21) is written for the unrelaxed frame, while equation (23) is for the fully saturated medium. An approximate equivalence between these equations can be established by applying Gassmann equation to both sides of equation (21). This is done in Appendix A, where we show that equation (23) is consistent with Gassmann equation.

3.1.2 Shear modulus

The dry-rock shear modulus μ_{m0} can be obtained from equations (7) by taking $\delta_c \to \infty$, so that $\delta_c/(1+\delta_c) \to 1$,

$$\frac{\mu_s}{\mu_{m0}} = 1 + \phi_p \frac{15(1-\nu_s)}{7-5\nu_s} + \left[\frac{16(1-\nu_s)}{15(1-0.5\nu_s)} + \frac{32(1-\nu_s)}{45}\right]\epsilon. \tag{25}$$

Subtracting this equation from (7) gives

$$\frac{\mu_s}{\mu_\infty} - \frac{\mu_s}{\mu_{m0}} = -\frac{32(1-\nu_s)}{45}\frac{\epsilon}{\delta_c+1}. \tag{26}$$

Similarly, for the bulk modulus, subtracting equation (16) from (19), we obtain

$$\frac{K_s}{K_{m\infty}} - \frac{K_s}{K_{m0}} = -\frac{16(1-\nu_s^2)}{9(1-2\nu_s)}\frac{\epsilon}{\delta_c+1}. \tag{27}$$

Combining equations (26) and (27) gives

$$\frac{1}{\mu_\infty} - \frac{1}{\mu_{m0}} = \frac{2K_s(1-2\nu_s)}{5\mu_s(1+\nu_s)}\left(\frac{1}{K_{m\infty}} - \frac{1}{K_{m0}}\right) \tag{28}$$

or

$$\frac{1}{\mu_\infty} = \frac{1}{\mu_{m0}} - \frac{4}{15}\left(\frac{1}{K_{m0}} - \frac{1}{K_{m\infty}}\right). \tag{29}$$

If the stiff pores are spherical, then the shear modulus of the rock without cracks is independent of the fluid compressibility, $\mu_\infty = \mu_{m\infty}$, and hence equation (29) is identical to equation (13).

3.1.3 Fluid effect in stiff pores

As discussed previously, if the stiff pores are spherical, the high-frequency limit wet-rock moduli predicted by the CPEM model are identical to those given by the MJG model. However, in real rocks, stiff pores are unlikely to have aspect ratio close to 1. More likely stiff pores could be approximated by spheroids with an aspect ratio a_s between 0.1 and 1 (or a range of aspect ratios). For bulk modulus, the KT approximation is consistent with Gasssman equation for a dilute concentration of spheroidal pores of any single aspect ratio. Indeed, the Gassmann theory assumes that the fluid pressure is the same in all the pores. Even though the KT theory assumes that pores are isolated, bulk compression will induce the same fluid pressure in all the spheroidal pores. However if stiff pores are a mix of spheroids with more than one aspect

ratio a_s (Zimmerman, 1991; Xu and White, 1995), the predictions of the KT and Gassmann equations will differ. In fact, the KT theory assumes that pores are isolated; hence the fluid pressure in pores of different aspect ratio will be different. Even if all pores are interconnected, in the high-frequency limit the fluid pressure will not have enough time to equilibrate, and hence in this limit the moduli should be consistent with the KT theory.

For the shear modulus, the high-frequency limit of the rock with stiff pores only computed using an effective medium theory (Kuster & ToksÃűz 1974; Berryman 1980) will deviate from the dry-rock modulus even when all of the stiff pores have a single aspect ratio $a_s \ll 1$. Indeed, this theory assumes that pores are isolated, and hence pressure induced by shear deformation in differently oriented spheroidal pores will be different. Thus, the resulting shear modulus will depend on the fluid compressibility unless all pores are spherical.

The high-frequency (or no-flow) limit predicted by the effective medium theory is only attained at frequencies above the characteristic frequency of squirt flow between stiff pores, $f_{sq} = a_s^3 \mu_s / \eta$ (Here a_s refers to the characteristic aspect ratio of a range or distribution of aspect ratios of pores), where η is dynamic viscosity of the pore fluid (Jones 1986; Gurevich et al. 2010). For a water-saturated quartz sandstone and $a_s = 0.2$, $f_{sq} \approx 3.5 \cdot 10^{11}$ Hz. Typical frequencies of ultrasonic rock-physics measurements are between 0.1 and 1 MHz, which are much smaller than f_{sq}. At these frequencies, fluid pressure will have ample time to equilibrate between stiff pores, and hence the moduli of the crack-free rock should be given by Gassmann equation. Hence, the contribution of stiff pores to the moduli should be computed with the Gassmann equation, as is done in the MJ and MJG models, rather than with any effective medium theory designed for isolated pores.

3.2 Comparison between the CPEM and EIASD models

The CPEM and MJG models are "non-interactive", that is, the effect of the compliant pores (cracks) on the elastic compliances is linear in crack density (or crack porosity). Hence, strictly speaking, these models are only valid for a dilute crack concentration, although Grechka & Kachanov (2006) showed numerically that non-interactive models often provide reasonable approximations for crack densities as high as 0.2.

In contrast, the EIAS model attempts to account for interaction between cracks, and thus the effect of cracks on the rock compliance is non-linear. Thus, the EIAS model will only agree with the CPEM for a dilute concentration of cracks. Below, we compare the dispersion predicted by the CPEM and EIASD models.

3.2.1 Bulk modulus

For the bulk modulus of fluid-saturated rocks, we rewrite the EIASD model by Endres & Knight (1997)(equation 48) as

$$\frac{K_s}{K_\infty} = 1 + \frac{K_s - K_f}{K_s}\left(\phi_p P_1 + \phi_c P_2\right). \tag{30}$$

Substituting the pore-shape factor P_2 from the second equation (3) gives

$$\frac{K_s}{K_\infty} = 1 + \phi_p \frac{K_s - K_f}{K_s} P_1 + \phi_c \frac{K_s - K_f}{K_f + \pi a \beta}. \tag{31}$$

On the other hand, the CPEM equation (6) gives

$$\frac{K_s}{K_\infty} = 1 + \phi_p \left[\frac{1}{\frac{3(1-\nu_s)}{2(1-2\nu_s)}\delta_p} + \frac{1}{\frac{3(1-\nu_s)}{2(1-2\nu_s)}}\right]^{-1} + \left[\frac{1}{\frac{16(1-\nu_s^2)}{9(1-2\nu_s)}\epsilon\delta_c} + \frac{1}{\frac{16(1-\nu_s^2)}{9(1-2\nu_s)}\epsilon}\right]^{-1}. \tag{32}$$

Furthermore, from equations (8) and (9), we have

$$\frac{3(1-\nu_s)}{2(1-2\nu_s)}\delta_p = \frac{3Y_s}{3(1-2\nu_s)}\left(\frac{1}{K_f} - \frac{1}{K_s}\right) = \frac{K_s - K_f}{K_f},$$

$$\frac{3(1-\nu_s)}{2(1-2\nu_s)} = \frac{3K_s + 4\mu_s}{4\mu_s}, \tag{33}$$

$$\frac{16(1-\nu_s^2)}{9(1-2\nu_s)}\epsilon = \frac{\phi_c K_s}{\pi a \beta}.$$

Substituting equations (18) and (33) into (32) gives

$$\frac{K_s}{K_\infty} = 1 + \phi_p \frac{(K_s - K_f)}{K_s} P_1 + \phi_c \frac{K_s - K_f}{K_f + \pi a\beta - \pi a\beta \frac{K_f}{K_s}}. \tag{34}$$

Equations (31) and (34) differ by a term using the first-order Taylor expansion

$$\Delta = \phi_c \frac{K_s - K_f}{K_s} \frac{\pi a \beta K_f}{(K_f + \pi a\beta)^2} \tag{35}$$

For a small aspect ratio a, the difference in equation (35) is always on the order of $a\phi_c$ and hence is negligible compared to the third term in equation (31), which is always on the order of $\frac{a}{\phi_c}$. Thus the EIASD and CPEM predictions for the bulk modulus are almost identical.

3.2.2 Shear modulus

For the shear modulus of fluid-saturated rocks, we rewrite the EIASD model by Endres & Knight (1997)(their equation 49) as

$$\frac{\mu_s}{\mu_\infty} = 1 + \phi\gamma = 1 + \phi_p Q_1 + \phi_c Q_2. \tag{36}$$

Substituting the pore-shape factor Q_2 from equation (3) gives

$$\frac{\mu_s}{\mu_\infty} = 1 + \phi_p Q_1 + \frac{8\mu_s\phi_c}{5\pi a(\mu_s + 2\beta)} + \frac{4}{15}\frac{\mu_s\phi_c}{K_f + \pi a\beta}\left(1 + \frac{3}{2}\frac{K_f}{\mu_s}\right) + \frac{\phi_c}{5}. \tag{37}$$

On the other hand, the CPEM equation (7) reads

$$\frac{\mu_s}{\mu_\infty} = 1 + \phi_p Q_1 + \left[\frac{16(1-\nu_s)}{15(1-0.5\nu_s)}\epsilon + \frac{32(1-\nu_s)}{45}\epsilon\left(1 + \frac{1}{\delta_c}\right)^{-1}\right]. \tag{38}$$

Furthermore, from equations (10) and $1 - \nu_s = \mu_s/(2\beta)$, we have

$$\begin{aligned} &\frac{16(1-\nu_s)}{15(1-0.5\nu_s)}\epsilon = \frac{8\mu_s\phi_c}{5\pi a(\mu_s + 2\beta)}, \\ &\frac{32(1-\nu_s)}{45}\epsilon\left(1 + \frac{1}{\delta_c}\right)^{-1} = \frac{4}{15}\phi_c\mu_s\frac{K_s - K_f}{K_s(\pi a\beta + K_f) - K_f\pi a\beta}. \end{aligned} \tag{39}$$

Using the identities (39) in (38) gives

$$\frac{\mu_s}{\mu_\infty} = 1 + \phi_p Q_1 + \frac{8\mu_s\phi_c}{5\pi a(\mu_s + 2\beta)} + \frac{4}{15}\mu_s\phi_c\frac{K_s - K_f}{K_s(\pi a\beta + K_f) - K_f\pi a\beta}. \tag{40}$$

If, as usually assumed, the aspect ratio a is small, then $\pi a\beta K_f \ll K_s K_f$, hence, equation (40) reduces to

$$\frac{\mu_s}{\mu_\infty} = 1 + \phi_p Q_1 + \frac{8\mu_s\phi_c}{5\pi a(\mu_s + 2\beta)} + \frac{4}{15}\frac{\mu_s\phi_c}{K_f + \pi a\beta}\left(1 - \frac{K_f}{K_s}\right). \tag{41}$$

Equations (37) and (41) differ by a term

$$\Delta = \frac{\phi_c}{5} + \frac{4}{15}\frac{\mu_s\phi_c K_f}{K_f + \pi a\beta}\left(\frac{3}{2\mu_s} + \frac{1}{K_s}\right). \tag{42}$$

For a small aspect ratio a, the crack porosity is also small and hence the term $\phi_c/5$ is always negligible. Furthermore, the second term in the right-hand side of (42) is on the order of $2\phi_c/3$ or smaller, and hence is also negligible. Thus the EIASD and CPEM predictions for the shear modulus are almost identical, with a relative difference on the order of the crack porosity.

The above analysis shows that the dispersion predicted by the three models (we compared the EIASD instead of the EIAS model for a dilute concentration of cracks) are almost identical with a very small difference. This consistency will be illustrated more clearly in the next section.

4 NUMERICAL COMPARISON OF DISPERSION MODELS

4.1 The dispersion index

Following equation (B.4), the bulk and shear dispersion indices are defined as

$$D_K = \frac{K_\infty - K_0}{2\sqrt{K_0 K_\infty}} \quad \text{and} \quad D_\mu = \frac{\mu_\infty - \mu_0}{2\sqrt{\mu_0\mu_\infty}}. \tag{43}$$

respectively, and are directly related to the bulk and shear quality factors. These indices, inspired by the Zener model described in Appendix B, are similar to those defined by Endres & Knight (1997), i.e., $D = (M_\infty - M_0)/M_0$.

The P-wave dispersion index is

$$D_P = \frac{E_\infty - E_0}{2\sqrt{E_0 E_\infty}}, \tag{44}$$

where

$$E = K + \frac{4}{3}\,\mu. \tag{45}$$

The S-wave dispersion index is $D_S = D_\mu$.

Assuming that M is the P-wave modulus, a dispersion index for the P-wave velocity can be defined from equation (B.5) as

$$D_v = \frac{v_\infty}{v_0} - 1 \approx \frac{1}{Q_P} = D_P, \tag{46}$$

where Q_P is the P-wave quality factor. A similar equation for the S wave can be obtained.

4.2 Parametrization of the models

In the three models discussed above, the MJG and CPEM models assume a small crack density. In contrast, the EIAS model is not restricted to a small crack density as it includes the interaction between cracks in some form. Indeed, the approach of Endres & Knight (1997) ensures that the EIAS predictions are always within the Hashin-Shtrikman bounds. However inclusion interactions, and hence accuracy of the EIAS model, depend on crack size distribution and the spatial distribution of crack centers.

Hence, in order to illustrate the similarities and differences of the dispersion predicted by the three models, we first compare the EIAS model and its dilute approximation—EIASD model. We then present the results of the comparison of the EIASD, MJG and CPEM models. The aim in this step is to make their parameters consistent. To this end, we assume that the dry-rock moduli K_{m0} and μ_{m0} in the MJG model are given by equation (5) of the EIASD model with $K_f = 0$. Also, K_h is the bulk modulus of the dry rock with pores only (no cracks) and hence should be given by the first of equations (5) with

$$K_h = \frac{K_s}{1 + \phi_p P_1}, \tag{47}$$

with P_1 is given by the first equation (3) and $K_f = 0$.

We assume that $K_s = \mu_s = 39$ GPa, $K_f = 2.25$ GPa (water) and $\phi = 0.1$. Numerical comparisons of the model predictions are presented in the next section.

4.3 Numerical results

The low- and high-frequency bulk (a) and shear (b) moduli predicted by the EIAS and EIASD models for $a = 0.001$ are displayed in Figure 1. The pore fluid is water. As can be seen, the EIASD model gives an almost same dispersion range for bulk modulus with values shifted up compared to the EIAS model but a narrow dispersion range for shear modulus. The bulk dispersion predicted by the EIAS and EIASD models is much higher than the shear dispersion.

Figure 2 shows the low- and high-frequency bulk (a) and shear (b) moduli of the water-saturated rocks predicted by the EIASD, MJG and CPEM models for $a = 0.001$. The normalized bulk and shear differences of the MJG and EIASD models relative to the CPEM model are presented in Figure 2c and d. As can be observed, in all cases, the low-frequency (relaxed) moduli are lower than the high-frequency (unrelaxed) ones as expected (the dispersion index should be positive). At low frequencies, the EIASD and MJG models have the same predictions for bulk and shear moduli compared to those given by the CPEM model. At high frequencies, the EIASD has the same prediction for bulk modulus but a smaller prediction for shear modulus compared to those given by the CPEM model when the crack density is relatively high. Different from the performance of the EIASD model, the MJG model gives a higher prediction for the bulk modulus but a smaller prediction for the shear modulus compared to those given by the CPEM model when the crack density is relatively high. These behaviours are demonstrated more clearly in Figure 2c and d, which are consistent with the previous analytical comparison in section 4.2. The agreement between the three models is very good also for other aspect ratios.

Figure 3 shows the bulk (a) and shear (b) dispersion indices predicted by the MJG model when the fluid is water, compared to those of the EIASD model. The differences at relatively high crack density, from a practical point of view, are actually small. Basically, the dispersion (and attenuation) increases with increasing crack density and decreases with increasing aspect ratio. Aspect ratios equal or greater than 0.1 show very weak attenuation, with bulk and shear quality factors $Q > 1/10^{-3} \approx 1000$. Although strictly not applicable due to the non-interaction assumption, it can be shown that for $\epsilon > 0.3$ all the three models show a very good agreement. Figure 3c and d shows the same data displayed in Figure 3a and b but in terms of the Zener quality factor, where it can clearly be seen that attenuation is higher for the smaller aspect ratio, i.e., a higher dispersion index.

Figure 4 compares the bulk (a) and shear (b) dispersion indices estimated from the EIASD and CPEM models. As can be seen, the two models yield very similar values, showing the consistency of the results by using two different theoretical approaches.

Figure 5 compares the bulk (a) and shear (b) dispersion indices by using the MJG (solid and dash lines) and (open circles and squares) MJ models when the fluid is gas, with K_f = 0.01 GPa, which roughly corresponds to methane at a pore pressure of 30 MPa and a depth of 3 km. As can be seen, the MJ model cannot be used for relatively high aspect ratios (e.g., say $a > 10^{-4}$), since it yields negative values of the dispersion index. This confirms the recognition that the original MJ model is valid only for liquid (Gurevich et al. 2009). Anelasticity for gas is weaker compared to water, i.e., for ϵ=0.1 and a = 0.001 the bulk quality factor is approximately 96 in Figure 5a (dash line), whereas it is 15 in Figure 3a.

Figure 6 shows the bulk (a), shear (b) and P-wave (c) dispersion indices of the MJG model (open circles) when the fluid is gas, compared to those of the EIASD model (solid lines). Dispersion and attenuation is lower than for water-saturated rocks (Figure 3), and is significant only at low aspect ratios and high crack density. Figure 6d shows the P-wave indices of the MJG model when the fluid is water, compared to those of the EIASD model. It shows similar characteristics as those of Figure 6c, with higher bulk and shear dispersion indices. It can be shown that the dispersion index of the P-wave velocity [equation (46)] is almost identical to that of the P-wave modulus E for $Q_P \gg 1$ (not shown).

It should be noted that the above comparisons are based on the assumption that the stiff pores are spherical. In real rocks stiff pores may have a lower aspect ratio, e.g., lie in a range $0.1 < a < 1$. For stiff pores in a shape of an oblate spheroid with an aspect ratio $a_s \leq 1$, the coefficients P_1 and Q_1 in the first and third equations (3) are

$$P_1 = \frac{1}{3}T_{iijj}, \quad \text{and} \quad Q_1 = \frac{1}{5}(T_{ijij} - P_1), \tag{48}$$

where T_{iijj} and T_{ijij} are given in Appendix A of Berryman (1980) or in page 189 of Mavko et al. (2009) (the inclusion moduli should be taken equal to zero).

The effect of the aspect ratio of the stiff pores on the bulk and shear moduli (a-b) and Zener quality factor (c-d) is illustrated in Figure 7. We compare the MJG results for spherical stiff pores ($a_s = 1$) and oblate spheroidal stiff pores ($a_s = 0.2$). The fluid is water. As can be observed, at constant crack density the dispersion and attenuation are weaker for decreasing aspect ratio of the stiff pores, and the low-frequency (relaxed) moduli are the same at high crack density. Figure 8 compares the MJG and EIASD models for $a_s = 0.2$. Both the moduli and quality factors (and dispersion indices as a consequence) are similar. Similar behaviours are obtained for the bulk and shear moduli.

5 CONCLUSIONS

We have performed a comparative analysis of Zener-based dispersion indices obtained with the generalised Mavko-Jizba relations, and two inclusion-based models that incorporate pore geometry and fluid pressure communication to model the elastic behaviour of porous rocks. The inclusion based models models are based on a combination of stiff (equant) pores and penny-shaped cracks. The low-frequency moduli correspond to full fluid pressure equilibration between cracks and pores, whereas at high frequencies the cracks are hydraulically isolated from pores. The difference between these two conditions results in significant moduli and velocity dispersion.

As demonstrated by the numerical comparisons, such dispersion (and attenuation) increases with crack density and decreases with increasing aspect ratio. Bulk modulus dispersion and attenuation are stronger than those for shear deformations. Aspect ratios equal or greater than 0.1 show very weak attenuation. Both analytical and numerical comparisons show that the three models yield very similar values, showing the consistency of the results by using two idealized theoretical approaches (EIASD and CPEM) compared to the MJG relations. Anelasticity for gas-saturated rocks is weaker than for liquid saturation. The dispersion indices can be viewed as a template to obtain the crack properties from low- and high-frequency velocity measurements.

Theoretical analysis and numerical examples show that when stiff pores are spherical and crack density is small, the predictions of all the models considered are almost identical. However when stiff pores are oblate spheroids with an aspect ratio less than 1 (say between 0.2 and 1), the high-frequency moduli predicted by inclusion-based models are considerably higher than the predictions of the MJG model. This is because the inclusion-based models assume that at high frequencies the pores are hydraulically isolated from each other, and hence correspond to the true high-frequency limit, which is attained at frequencies of 10^9 Hz or higher, which are irrelevant for measurements on rocks. In contrast, in the MJG model, the effect of stiff pores is modeled with Gassmann's theory, and hence its high-frequency limit corresponds to a case where pores are assumed disconnected from cracks, but interconnected with each other. Our analysis shows that these assumptions of the MJG model hold at ultrasonic frequencies on the order of 10^6 Hz. The two inclusion based models can be easily made consistent with the MJG model by accounting for the effect of fluid in stiff pores using Gassmann's theory.

Since predictions of all the three models are very similar, the preference for one model or another is a matter of convenience. When the specific pore space geometry is known or

assumed, the inclusion based models would be preferred (but the effect of fluid in stiff pores should be treated with Gassmann's theory). Of the inclusion based model, the non-interactive models are simpler and hence preferred when the crack density is low, but the EIAS model must be used for high crack densities. Conversely, when not much is known about pore geometry, the MJG model would be the most logical choice.

REFERENCES

Adelinet, M., Fortin, J., & Guéguen, Y., 2011. Dispersion of elastic moduli in a porous-cracked rock: Theoretical predictions for squirt-flow, *Tectonophysics*, **503**(1), 173–181.

Alkhimenkov, Y., Caspari, E., Gurevich, B., Barbosa, N. D., Glubokovskikh, S., Hunziker, J., & Quintal, B., 2020. Frequency-dependent attenuation and dispersion caused by squirt flow: Three-dimensional numerical study, *Geophysics*, **85**(3), 129–145.

Berryman, J. G., 1980. Long-wavelength propagation in composite elastic media ii. ellipsoidal inclusions, *J. Acoust. Soc. Am.*, **68**(6), 1820–1831.

Biot, M. A., 1962. Mechanics of deformation and acoustic propagation in porous media, *J. Appl. Phys.*, **33**(4), 1482–1498.

Brown, R. J. S. & Korringa, J., 1975. On the dependence of the elastic properties of a porous rock on the compressibility of the pore fluid, *Geophysics*, **40**(4), 608–616.

Carcione, J. M., 2014. *Wave Fields in Real Media:Theory and numerical simulation of wave propagation in anisotropic, anelastic, porous and electromagnetic media*, Elsevier.

Carcione, J. M. & Gurevich, B., 2011. Differential form and numerical implementation of BiotâĂŹs poroelasticity equations with squirt dissipation, *Geophysics*, **76**(6), N55–N64.

Carcione, J. M., Cavallini, F., Ba, J., Cheng, W., & Qadrouh, A. N., 2019. On the kramers-kronig relations, *Rheol Acta*, **58**(1), 21–28.

Chapman, M., Zatsepin, S. V., & Crampin, S., 2002. Derivation of a microstructural poroelastic model, *Geophys. J. Int.*, **151**(2), 427–451.

Dvorkin, J., Mavko, G., & Nur, A., 1995. Squirt flow in fully saturated rocks, *Geophysics*, **60**(1), 97–107.

Endres, A. L. & Knight, R. J., 1997. Incorporating pore geometry and fluid pressure communication into modeling the elastic behavior of porous rocks, *Geophysics*, **62**(1), 106–117.

Eshelby, J. D., 1957. The determination of the elastic field of an ellipsoidal inclusion, and related problems, *Proc. Roy. Soc. London. Ser.A*, **241**(1226), 376–396.

Gassmann, F., 1951. Über die Elastizität poröser Medien, *Veirtel. Naturforsch. Ges. Zürich*, **96**, 1–23.

Grechka, V. & Kachanov, M., 2006. Effective elasticity of fractured rocks, *Lead. Edge*, **25**(2), 152–155.

Gurevich, B., 2003. Elastic properties of saturated porous rocks with aligned fractures, *J. Appl. Geophys.*, **54**(3), 203–218.

Gurevich, B., Makarynska, D., & Pervukhina, M., 2009. Ultrasonic moduli for fluid-saturated rocks: Mavko-jizba relations rederived and generalized, *Geophysics*, **74**(4), N25–N30.

Gurevich, B., Makarynska, D., de Paula, O. B., & Pervukhina, M., 2010. A simple model for squirt-flow dispersion and attenuation in fluid-saturated granular rocks, *Geophysics*, **75**(6), N109–N120.

Jones, T., 1986. Pore fluids and frequencyâĂŘdependent wave propagation in rocks, *Geophysics*, **51**(10), 1939–1953.

Kachanov, M., 1993. Elastic solids with many cracks and related problems, in *Advances in applied mechanics*, vol. 30, pp. 259–445, Elsevier.

Kuster, G. T. & ToksÃűz, M. N., 1974. Velocity and attenuation of seismic waves in twoâĂŘphase media: Part i. theoretical formulations, *Geophysics*, **39**(5), 587–606.

Mavko, G. & Jizba, D., 1991. Estimating grain-scale fluid effects on velocity dispersion in rocks, *Geophysics*, **56**(12), 1940–1949.

Mavko, G. & Nur, A., 1975. Melt squirt in the aesthenosphere, *Geophys. J. Int.*, **80**(11), 1444–1448.

Müller, T. M., Gurevich, B., & Lebedev, M., 2010. Seismic wave attenuation and dispersion resulting from wave-induced flow in porous rocks–a review, *Geophysics*, **75**(5), 75A147–75A164.

Murphy III, W., Winkler, K., & Kleinberg, R., 1986. Acoustic relaxation in sedimentary rocks-dependence on grain contacts and fluid saturation, *Geophysics*, **51**(3), 757âĂŞ–766.

O'Connell, R. J. & Budiansky, B., 1977. Viscoelastic properties of fluid-saturated cracked solids, *J. Geophys. Res.*, **82**(36), 5719–5735.

Palmer, I. & Traviola, M., 1980. Attenuation by squirt flow in undersaturated gas sands, *Geophysics*, **45**(12), 1780âĂŞ–1792.

Pride, S. R., Berryman, J. G., & Harris, J. M., 2004. Seismic attenuation due to wave-induced flow, *J. Geophys. Res.*, **109**(B1).

Walsh, J. B., 1965. The effect of cracks on the compressibility of rock, *J. Geophys. Res.*, **70**(2), 381–389.

Zhang, L., Ba, J., Carcione, J. M., & Sun, W., 2019a. Modeling wave propagation in cracked porous media with penny-shaped inclusions, *Geophysics*, **84**(4), WA141–WA151.

Zhang, L., Ba, J., Fu, L., Carcione, J. M., & Cao, C., 2019b. Estimation of pore microstructure by using the static and dynamic moduli, *Int. J. Rock. Mech. Min.*, **113**, 24–30.

Zimmerman, R. W., 1991. *Compressibility of Sandstones*, Elsevier, Amsterdam.

APPENDIX A: WET-ROCK BULK MODULUS BASED ON THE UNRELAXED MJG MODULUS

To verify if equations (23) and (14) are equivalent, we need to rewrite equation (23) for a saturated medium. A wet-rock modulus K_∞ for a medium with a high-frequency unrelaxed bulk modulus $K_{m\infty}$, is given by the Gassmann equation

$$K_\infty = K_{m\infty} + K_h S(K_{m\infty}), \tag{A.1}$$

where $S(K_{m\infty}) = \alpha^2 M/K_h$, $\alpha = 1 - K_{m\infty}/K_s$, and $M = K_s/\left[(1 - K_{m\infty}/K_s)/K_s - \phi(1 - K_s/K_f)\right]$ (e.g., Carcione, 2014).

We know that for most rocks $K_f \ll K_m$ and hence the Gassmann correction to the unrelaxed modulus [the second term in the right-hand side of equation (A.1)] is small compared to the first term. We can make this fact explicit by introducing a small parameter δ into equation (A.1),

$$K_\infty = K_{m\infty} + \delta K_h S(K_{m\infty}). \tag{A.2}$$

Note also that by construction the second term in the right-hand side of equation (14) is very small, so that we can write

$$K_{m\infty} \approx K_h(1 + \varepsilon_h). \tag{A.3}$$

where $\varepsilon_h = K_h\phi_c(1/K_s - 1/K_f) \ll 1$. Substitution of equation (A.3) into equation (A.2) gives

$$K_\infty = K_h\left(1 + \varepsilon_h + \delta S\left[K_h(1 + \varepsilon)\right]\right). \tag{A.4}$$

Expanding $S[K_h(1 + \varepsilon_h)]$ in powers of ε_h yields

$$K_\infty = K_h\left(1 + \varepsilon_h + \delta\left[(S(K_h) + \varepsilon_h S_1\right]\right), \tag{A.5}$$

or

$$K_\infty = K_h(1 + \varepsilon_h + \delta S(K_h) + \delta\varepsilon_h S_1). \tag{A.6}$$

The last term in equation (A.6) contains a product of two small parameters and hence can be neglected, thus equation (A.6) reduces to

$$K_\infty = K_h\left[1 + \varepsilon_h + \delta S(K_h)\right]. \tag{A.7}$$

Considering $K_h^{sat} = K_h[1 + \delta S(K_h)]$ equation (A.7) simplifies to

$$K_\infty = K_h^{sat} + \varepsilon_h K_h = K_h^{sat}\left(1 + \varepsilon_h \frac{K_h}{K_h^{sat}}\right). \tag{A.8}$$

Similar to ε_h , we define $\varepsilon_h^{sat} = K_h^{sat}\phi_c(1/K_s - 1/K_f) \ll 1$ and obtain

$$K_\infty = K_h^{sat}\left(1+\varepsilon_h\frac{K_h}{K_h^{sat}}\right) = K_h^{sat}\left[1+\varepsilon_h^{sat}\left(\frac{K_h}{K_h^{sat}}\right)^2\right]. \tag{A.9}$$

Since $\varepsilon_h^{sat} \ll 1$ and $K_h/K_h^{sat} \approx 1-\delta S(K_h)$, equation (A.9) reduces to

$$K_\infty = K_h^{sat}(1+\varepsilon_h^{sat}). \tag{A.10}$$

Equation (A.10) approximates to equation (23).

APPENDIX B: THE ZENER MODEL

A classical model of viscoelastic behaviour is the Zener model, which is defined by the complex modulus

$$M(\omega) = M_\infty - \frac{M_\infty - M_0}{1+i\omega\tau}, \tag{B.1}$$

where ω is the angular frequency, τ is a relaxation time, $M_0 = M(0)$ and $M_\infty = M(\infty)$ are the relaxed and unrelaxed moduli (low and high frequency, respectively), $i=\sqrt{-1}$, and $M_\infty \geq M_0$ holds (Carcione 2014, e.g.). The Zener model satisfies the Kramers-Kronig relations (Carcione et al. 2019, e.g.). Function $(M-M_\infty)(\omega)$ has a unique pole in the upper half ω-plane, i.e., at i/ω and therefore it is analytic in the lower half ω-plane as required by causality. Its inverse time Fourier transform is causal and smooth for $t>0$, since it is basically an exponential function of time.

The quality factor is defined as

$$Q(\omega) = \frac{M_\mathrm{R}}{M_\mathrm{I}} = \frac{M_0+M_\infty(\omega\tau)^2}{\omega\tau(M_\infty-M_0)} \tag{B.2}$$

(e.g. Carcione 2014, p.91) which has the minimum value

$$Q_0 = \frac{2\sqrt{M_\infty M_0}}{M_\infty - M_0} = \frac{2v_\infty v_0}{v_\infty^2 - v_0^2} \tag{B.3}$$

(Carcione 2014, p.96), where we have defined the phase velocities at zero and infinite frequency as v_0 and v_∞, such that $M_0=\rho v_0^2$ and $M_\infty = \rho v_\infty^2$, where ρ is the mass density.

Let us define the Zener dispersion index as the inverse of the minimum quality factor, or dissipation factor, as

$$D = \frac{1}{Q_0} = \frac{M_\infty - M_0}{2\sqrt{M_\infty M_0}} = \frac{v_\infty^2 - v_0^2}{2v_\infty v_0} \tag{B.4}$$

It is easy to show that the amount of velocity dispersion is

$$\Delta v = v_\infty - v_0 = v_0\left(Q_0^{-1} + \sqrt{1+Q_0^{-2}} - 1\right) \approx \frac{v_0}{Q_0}, \tag{B.5}$$

where the approximation holds for low-loss solids ($Q_0 \gg 1$). This is a simple relation between

the maximum velocity dispersion and the minimum Q (higher attenuation). The Kramers-Kronig relations are more general and reflect the fact that if velocity dispersion is known for all frequencies then Q is known for all frequencies and vice versa.

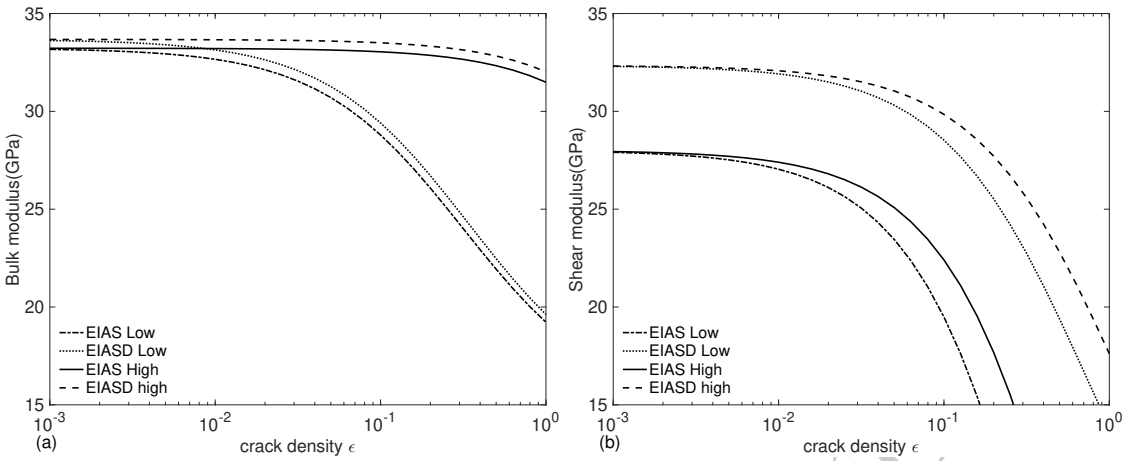

Figure 1. Comparison between the EIAS (dash-dotted and solid lines) and EIASD (dotted and dashed lines) low- and high-frequency bulk(a) and shear(b) moduli as a function of the crack density and an aspect ratio $a = 0.001$. The fluid is water.

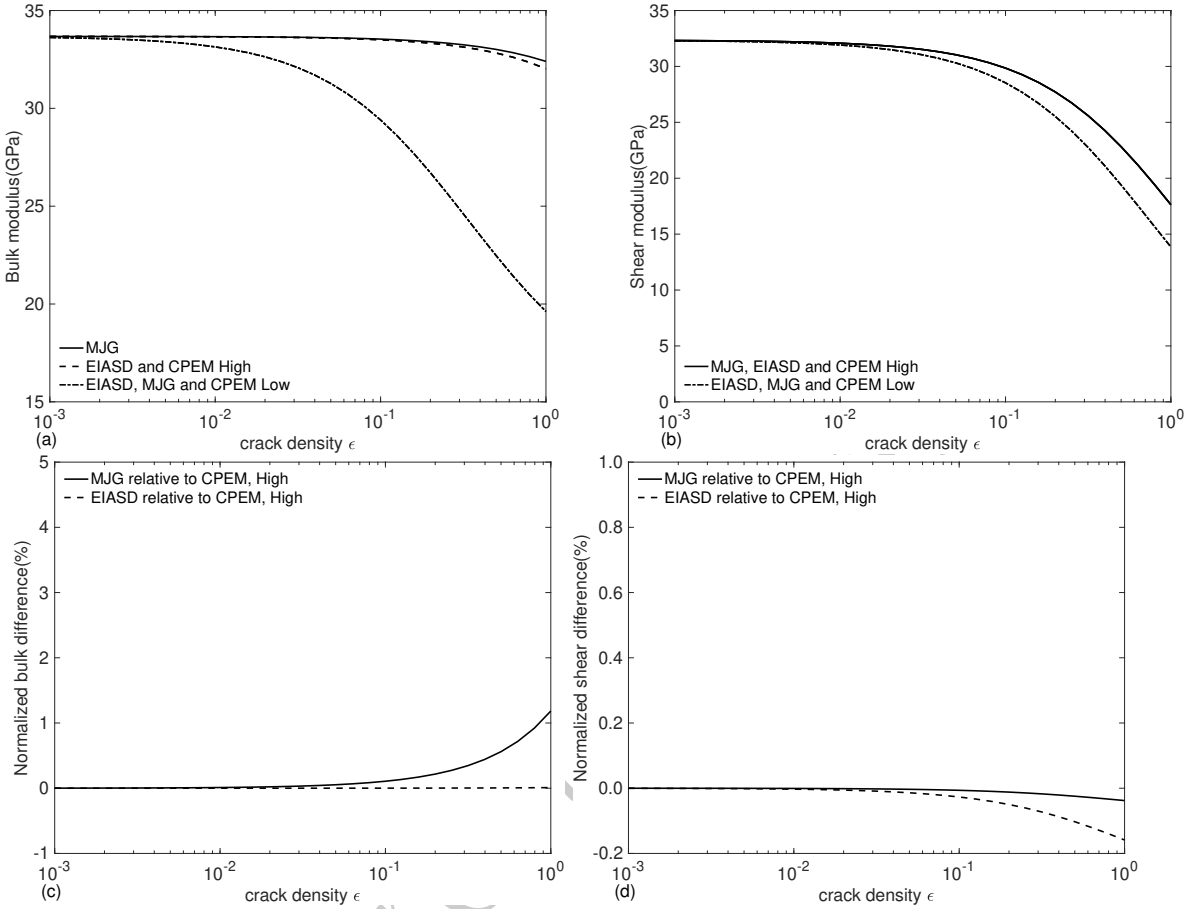

Figure 2. Comparison between the MJG, EIASD and CPEM low- and high-frequency bulk (a) and shear (b) moduli as a function of the crack density and an aspect ratio $a = 0.001$. (c) and (d) correspond to the normalized bulk and shear differences of the MJG and EIASD models in high-frequency limits relative to those given by the CPEM model. The fluid is water.

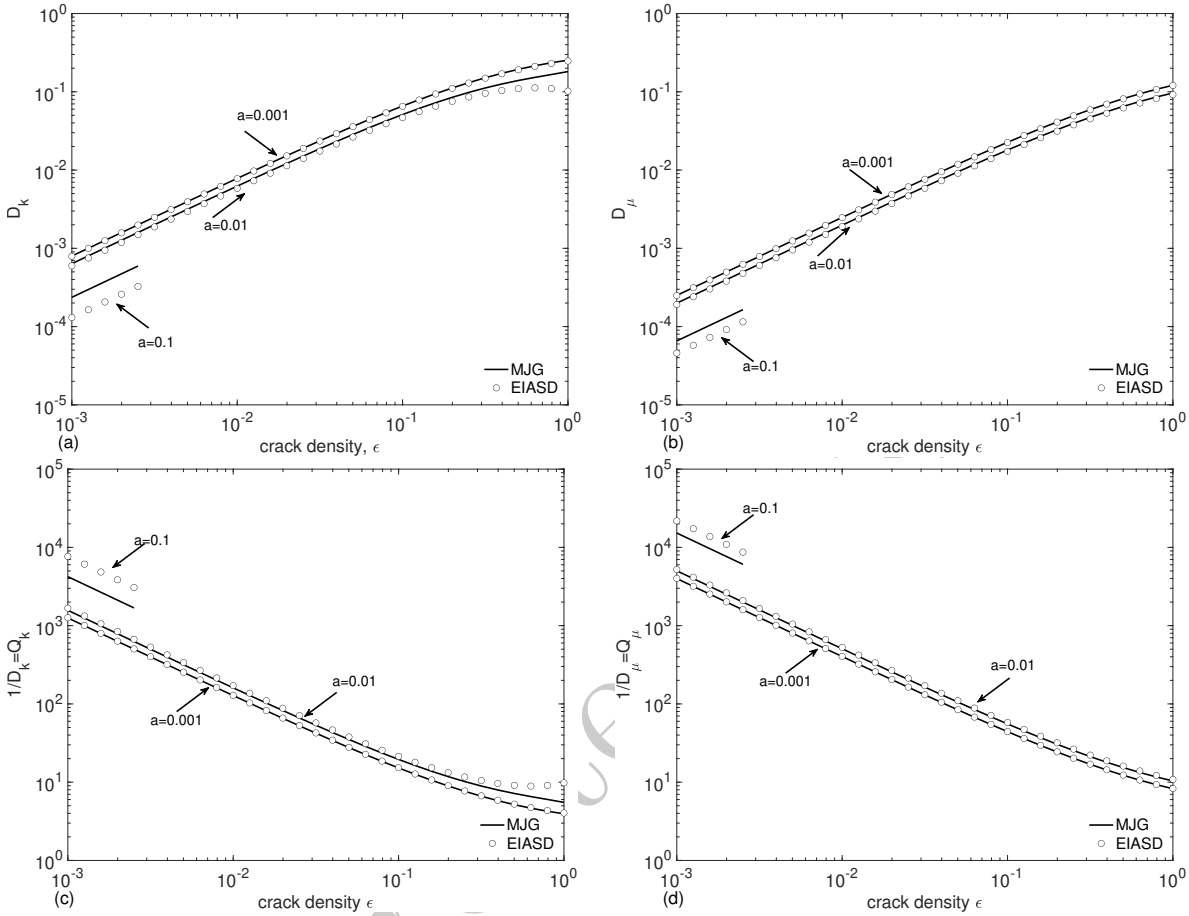

Figure 3. Comparison between the EIASD (circles) and MJG (lines) bulk and shear dispersion indices (a-b) and their Zener quality factors (c-d) as a function of the crack density and three values of the aspect ratio a. The fluid is water.

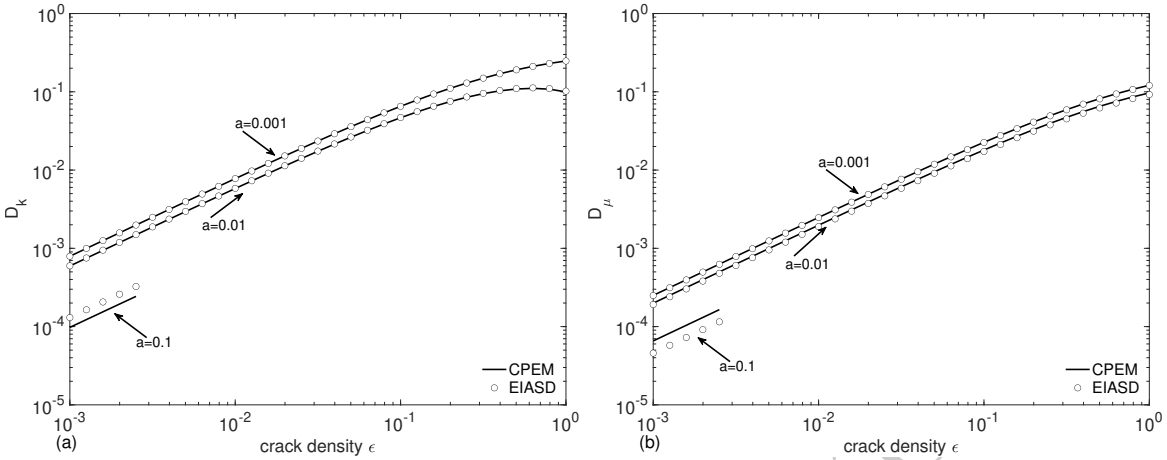

Figure 4. Comparison between the EIASD (circles) and CPEM (lines) bulk (a) and shear (b) dispersion indices as a function of the crack density and three values of the aspect ratio. The fluid is water.

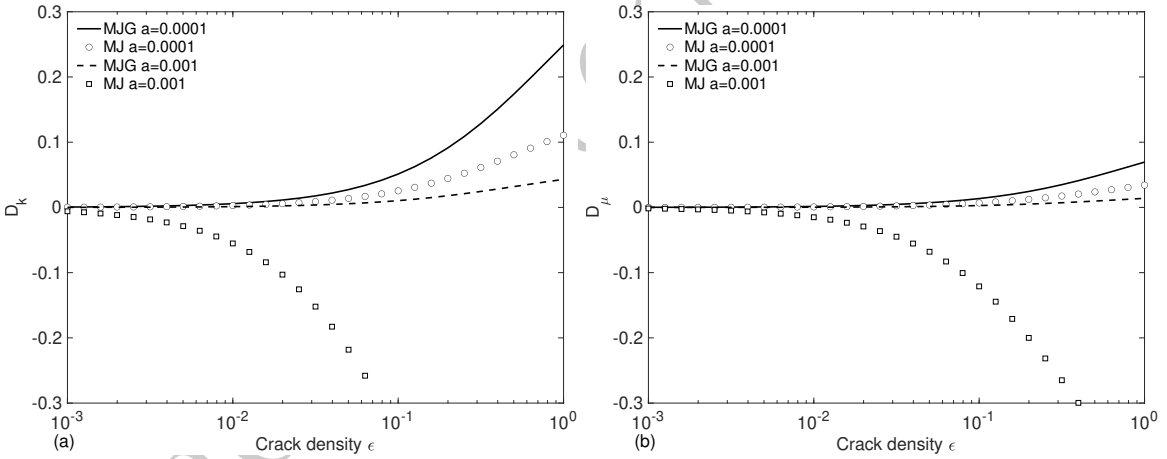

Figure 5. Comparison between the MJG (solid an dash lines) and original MJ (open circles and squares) bulk (a) and shear (b) dispersion indices as a function of crack density and two values of the aspect ratio. The fluid is gas. The open squares with $a = 10^{-3}$ represent unphysical values, since the dispersion index is negative

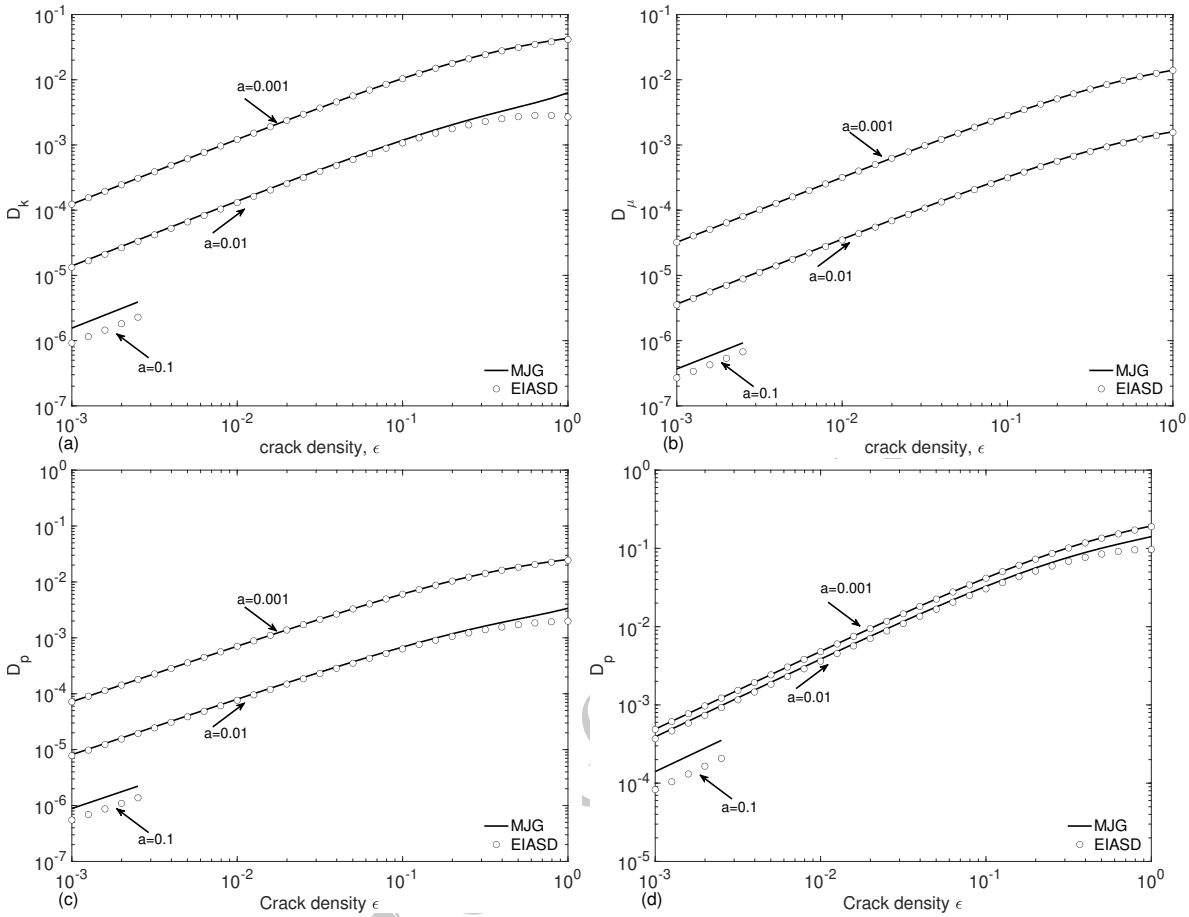

Figure 6. Comparison between the EIASD (circles) and MJG (lines) bulk (a), shear (b) and P-wave (c) dispersion indices as a function of crack density and three values of the aspect ratio. The fluid is gas. Figure 6(d) is the P-wave dispersion indices for water-saturated condition.

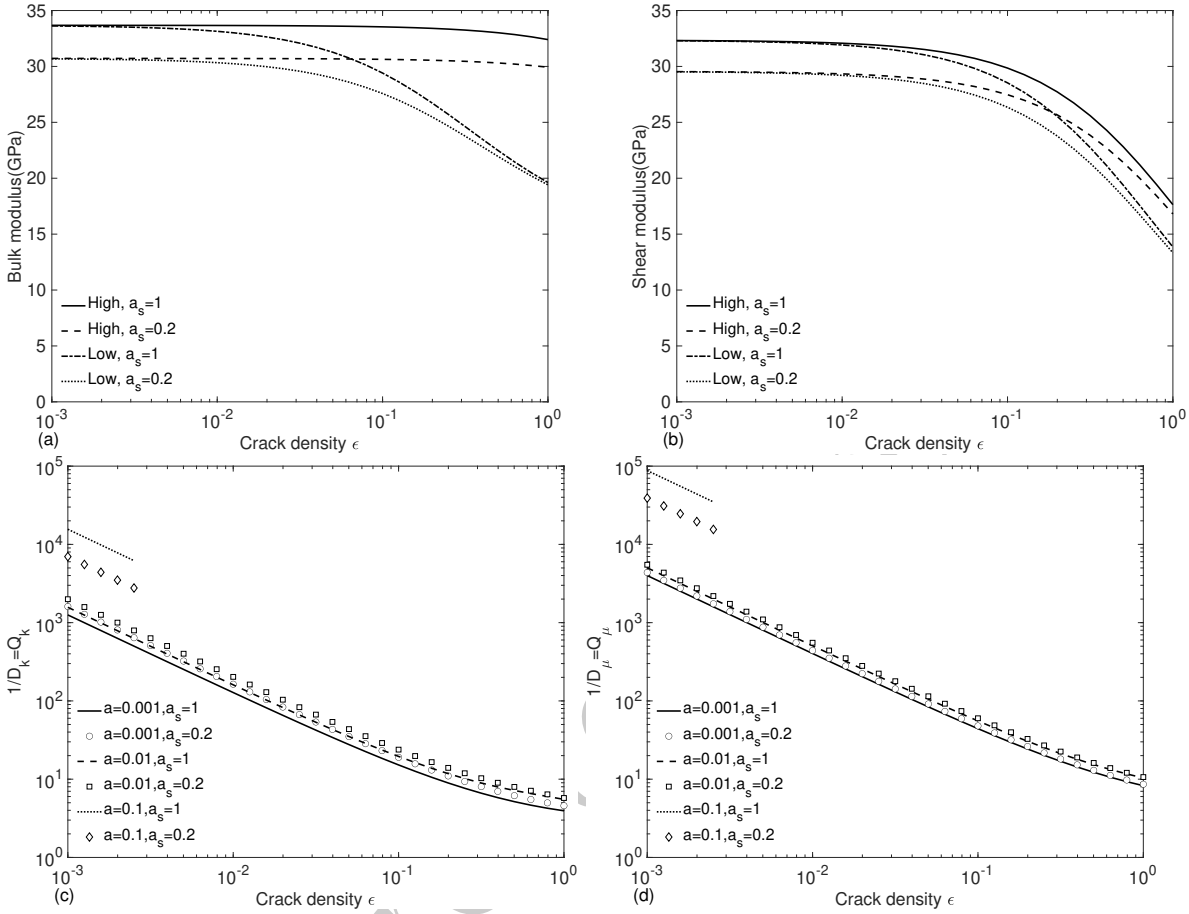

Figure 7. Effect of the aspect ratio of the stiff pores, a_s, on the low (relaxed) and high (unrelaxed) bulk (a) and shear (b) moduli and bulk (c) and shear (d) quality factors. The aspect ratio of the cracks in Figure 7(a) and (b) is $a = 10^{-3}$ and the fluid is water. The model is based on the MJG relations.

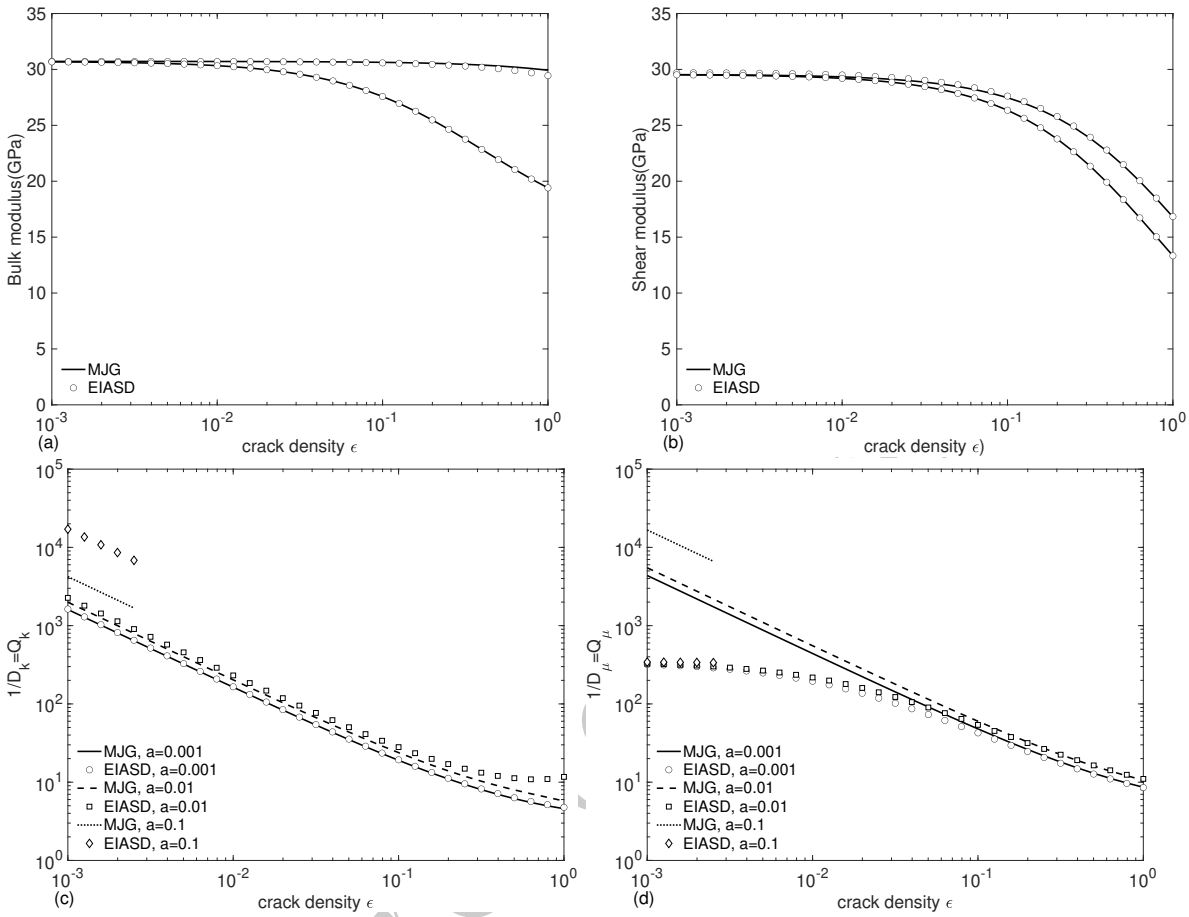

Figure 8. Comparison between the EIASD (symbols) and MJG (lines) bulk (a), shear (b) moduli and bulk (c) and shear (d) quality factors as a function of crack density and three values of the aspect ratio. The aspect ratio of the stiff pores is $a_s = 0.2$ and the aspect ratio of the cracks in Figure 8(a) and (b) is $a = 10^{-3}$. The fluid is water.